

The measurement of the splashback radius of dark matter halo

WEIWEI XU,^{1,2,3,*} HUANYUAN SHAN,^{4,5,6,†} RAN LI,^{1,2,7} JI YAO,⁴ CHUNXIANG WANG,^{1,2,7} NAN LI,¹ AND CHAOLI ZHANG⁸

¹*National Astronomical Observatories (NAOC), Chinese Academy of Sciences, Beijing 100101, China*

²*Institute for Frontiers in Astronomy and Astrophysics, Beijing Normal University, Beijing 102206, China*

³*The Kavli Institute for Astronomy and Astrophysics, Peking University (KIAA-PKU), Beijing 100871, China*

⁴*Shanghai Astronomical Observatory (SHAO), Nandan Road 80, Shanghai 200030, China*

⁵*Key Laboratory of Radio Astronomy and Technology, Chinese Academy of Sciences, A20 Datun Road, Chaoyang District, Beijing, 100101, P. R. China*

⁶*University of Chinese Academy of Sciences, Beijing 100049, China*

⁷*School of Astronomy and Space Science, University of Chinese Academy of Science, Beijing 100049, China*

⁸*College of Computer Science and Artificial Intelligence, Wenzhou University, 325035 Wenzhou, China*

ABSTRACT

In the hierarchical evolution framework of cosmology, larger halos grow through matter accretion and halo mergers. To clarify the halo evolution, we need to define the halo mass and radius physically. However, the pseudo-evolution problem makes the process difficult. Thus, we aim to measure the splashback radius, a physically defined halo radius for a large number of halos with various mass and redshift, and to determine the most important parameters to affect it. We use the typical definition of splashback radius as the radius with the steepest radial density profile. In this work, we measure the splashback radius (R_{sp}) of dark matter halos within the mass of $10^{13}M_{\odot}$ to $3 \times 10^{15}M_{\odot}$ and redshifts spanning 0.08 to 0.65. This is the measurement of the R_{sp} in the largest range of halo mass and redshift. Using the shear catalog of the DECaLS DR8, we investigate the splashback radius of halos associated with galaxies and galaxy clusters identified in the various catalogs. Our finding reveals a trend wherein massive halos demonstrate a larger splashback radius, and the normalized splashback radius ($R_{\text{sp}}/R_{200\text{m}}$) shows a U-shaped mass evolution. The upturn in these relations mainly comes from the contribution of massive halos with low redshifts. We further find the splashback radius increases with the peak height, while the normalized splashback radius has a negative relation with the peak height. We also find the $R_{\text{sp}} \gtrsim R_{200\text{m}}$ for most halos, indicating their low accretion rates. Our result is consistent with previous literature across a wide range of mass, redshift, and peak height, as well as the simulation work from [More et al. \(2015\)](#).

Keywords: weak gravitational-lensing: general catalogs-surveys-galaxy cluster

1. INTRODUCTION

In the standard Λ CDM cosmological framework, cosmic structures grow through a hierarchical process ([Gunn & Gott 1972](#)). The formation of substantial dark matter halos originates from the initial high-density peak in the early universe ([Fillmore & Goldreich 1984](#)). As matter accumulates in the region, a deep gravitational well forms, performing a large attraction to nearby materials. Finally, a large dark matter halo forms. Once the outer boundary of the dark matter halo

is well-defined, the halo mass is constrained, which is the most important parameter of the dark matter halo.

A natural question arises regarding how to define the outer boundary of the dark matter halo. Commonly employed radii include the virial radius and the radii defined with the overdensity, such as R_{500} and R_{200} . Nonetheless, these radii likely suffer from the pseudo-evolution of the halo mass, as demonstrated in [Diemer et al. \(2013\)](#). This phenomenon results in two identical halos located at different redshifts appearing to possess varying masses, due to the redshift evolution of the cosmological critical density. Consequently, it is vital to establish a physically-motivated boundary of the halo to accurately characterize the evolution of the dark mat-

* wxu@pku.edu.cn

† hyshan@shao.ac.cn

ter halo (Diemer & Kravtsov 2014; Adhikari et al. 2014; More et al. 2015). Furthermore, the dependence of assembly bias on halo mass definitions is closely linked to the radius definition, due to the dependence of halo clustering on halo property other than mass (More et al. 2016; Villarreal et al. 2017; Chue et al. 2018; Mansfield & Kravtsov 2020).

The splashback radius (R_{sp}) is one of the physically motivated radii of dark matter halo. Within the framework of the self-similar spherical collapse model, the dark matter halos can be characterized by a set of infinitesimally thin mass shells. These shells are initially coupled with the Hubble flow, undergoing accelerated expansion before decelerating, turning around, and collapsing into the halo, and eventually virializing under the influence of gravitational forces (Fillmore & Goldreich 1984; Bertschinger 1985). The splashback radius is thus defined as the boundary separating virialized and infalling shells. Particle apocenter scattering (Adhikari et al. 2014; Mansfield et al. 2017) implies that halos and the splashback radii may not be perfectly spherical, and it is also influenced by the energy and momentum of particles as they begin to infall (Diemer et al. 2017). In the simulation, the splashback radius is estimated with the apocenter of the accreted dark matter particles in their first orbit motion (Diemer et al. 2017). The work of Pizzardo et al. (2023) also confirms with IllustrisTNG simulation that the splashback radius effectively labels the inner boundary of the region where infalling matter dominates.

For simplicity, the location with the steepest slope of 3D density profile $\rho(r)$ is usually taken as the splashback radius, especially in observations (e.g., Diemand & Kuhlen 2008; Cuesta et al. 2008; More et al. 2015). In More et al. (2015), the small radial velocity near the apocenter results in the accreted matter piling up in the nearby region, and further the density enhancement caused a caustic in the splash-back area. Thus, the splashback radius, defined as the orbital apocenter of the accreted matter, corresponds to the outermost caustic. In the spherical collapse model, the halo within the splashback radius includes approximately all material ever accreted, thus the change of M_{sp} comes from the new accreted matter, which is barely affected by the pseudo-evolution.

Using the splashback radius as a proxy for the halo boundary, it is possible to distinguish discrepancies in the assembly bias measurements (Chue et al. 2018). Additional researches (Adhikari et al. 2016, 2018; Banerjee et al. 2020) indicate that the splashback radius may serve as a tool for assessing dynamical friction and constraining alternative theories for gravity and self-

interacting dark matter. Apart from the splashback radius, other radii have been proposed for various purposes. For instance, Fong et al. (Fong & Han 2021; Fong et al. 2022) have employed the depletion radius relating to the halo bias and infalling velocity to describe the depleted area of growing halos, which is approximately 2.5 times of the virial radius and 1.7–3 times of the splashback radius.

Many works have been dedicated to measuring the splashback radius. The first detection of the splashback radius was made by More et al. (2016). They measure the surface density profile around redMaPPer (Rykoff et al. 2014) clusters from the Sloan Digital Sky Survey (SDSS) Data Release 8 (DR8), and find the model with splashback radius (Diemer & Kravtsov 2014) fits the profile better than the model without this feature. Then, in the work of Baxter et al. (2017), redMaPPer clusters display an abrupt decrease of the fraction of red galaxies around the location of the splashback radius. In Chang et al. (2018), they measure the splashback radius with the galaxy number density and weak lensing mass profiles of the redMaPPer clusters from first-year Dark Energy Survey (DES) data. They use the same method with the work of More et al. (2016) and Baxter et al. (2017), and obtain consistent results with them. Their measurements are also consistent with Λ CDM simulations. In addition, they conclude the r_{sp} scales with $R_{200\text{m}}$ and it does not evolve with redshift within the redshift of 0.3–0.6. Then, the splashback radius is detected for more optically selected clusters (Murata et al. 2020; Bianconi et al. 2021; Contigiani et al. 2023), Sunyaev-Zel’dovich effect (SZ)-selected clusters (Shin et al. 2019, 2021; Zürcher & More 2019), intra-cluster light of clusters (Deason et al. 2021). In addition, multiple works investigate splashback radius in simulations (such as Xhakaj et al. 2020).

In multiple works (e.g., Diemer & Kravtsov 2014; More et al. 2015; Chang et al. 2018), the splashback radius is typically defined or measured as the radius with the steepest density slope (called R_{steep} in this paragraph for convenience). However, some recent works (e.g., Aung et al. 2021; Diemer 2022; García et al. 2023) find the splashback radius is not necessarily the same with R_{steep} , especially for less massive halos. In less massive halos, splashback features are weaker because of their lower mass accretion rates on average. Besides, their splashback features occur at a larger radius, where the infalling term becomes important or even dominates. In this situation, R_{steep} is the radius where the steep inner profile and shallow outer profile trade-off. However, to keep consistent with previous relevant works, we keep

the typical way to define and characterize the splashback radius, as $R_{\text{sp}} = R_{\text{steep}}$, in this work.

In this paper, we measure the halo splashback radius with the galaxy-galaxy lensing method, encompassing halo mass between 10^{13} and $3 \times 10^{15} M_{\odot}$ and a redshift range of $0.08 - 0.65$. Throughout the paper, we adopt $M_{200\text{m}}$ and $c_{200\text{m}}$ as the mass and concentration of the halo and use the comoving distance.

The cosmological parameters used in this paper are obtained from [Planck Collaboration et al. \(2020\)](#), consisting of the Hubble constant $H_0 = 67.4 \text{ km s}^{-1} \text{ Mpc}^{-1}$, baryon density parameter $\Omega_b h^2 = 0.0224$, cold dark matter density parameter $\Omega_{\text{cdm}} h^2 = 0.120$, matter fluctuation amplitude $\sigma_8 = 0.811$, power index of primordial power spectrum $n_s = 0.965$, and matter density parameter $\Omega_m = 0.315$. This paper is organized as follows: Sec. 2 introduces the source and lens catalogs; Sec. 3 presents the lensing signal, lensing model, and associated systematics; Sec. 4 shows and discusses the results. We describe the conclusion in Sec. 5.

2. DATA

2.1. Source catalog

In our measurement of the lensing signal, we use the shear catalog from the Dark Energy Camera Legacy Survey Data Release 8 catalog (DECaLS DR8) covering a sky area of $9,500 \text{ deg}^2$, as a part of the Dark Energy Spectroscopic Instrument Legacy Imaging Survey ([Blum et al. 2016](#); [Dey et al. 2019](#)). The shear catalog is obtained mainly with the following steps.

- In the shear measurement, five morphologies are used to describe and divide the *Tractor* source ([Lang et al. 2016](#)). The models include point sources, round exponential galaxies with a variable radius, DeVaucouleurs, exponential, and the composite model. The DECaLS DR8 sources below the 6σ detection limit in all stacks are removed.
- A joint fitting on the optical images (in g , r , and z bands) is used to estimate the ellipticity of a galaxy.
- We estimate the photometric redshift of galaxy with the k -nearest-neighbour algorithm (kNN, [Zou et al. 2019](#)). For reliability, we use not only the three optical bands (g , r , and z), but also two infrared bands ($W1$ and $W2$) from the Wide-Field Infrared Survey Explorer, and only reserve the galaxies with $r < 23 \text{ mag}$. This way, we obtain the catalog of about 2.2 million galaxies with photometric redshifts.

Table 1. The bin criteria of lens samples.

Cat.	bin	z	Mass proxy	Num.*
RM	z1m1	0.08 – 0.36	20 – 34	2,484
	z1m2	0.08 – 0.36	34 – 60	2,474
	z2m1	0.36 – 0.65	20 – 39	3,130
	z2m2	0.36 – 0.65	39 – 60	3,031
ZOU21	z1m1	0.23 – 0.43	13.90 – 14.10	57,998
	z1m2	0.23 – 0.43	14.10 – 14.40	49,119
	z2m1	0.43 – 0.58	13.90 – 14.10	55,704
	z2m2	0.43 – 0.58	14.10 – 14.40	58,365
YANG21	z1m1	0.25 – 0.41	13.50 – 13.67	36,270
	z1m2	0.25 – 0.41	13.67 – 14.00	36,646
	z2m1	0.41 – 0.53	13.50 – 13.67	39,502
	z2m2	0.41 – 0.53	13.67 – 14.00	41,848
CMASS	m1	0.35 – 0.65	11.00 – 11.50	378,884
	m2	0.35 – 0.65	11.50 – 12.00	338,123
LOWZ	m1	0.10 – 0.35	11.25 – 11.50	133,934
	m2	0.10 – 0.35	11.50 – 11.75	103,829

Note. The first two columns are the catalog name and the bin name. In the bin name, the ‘m1’ and ‘m2’ represent less and more massive bins, ‘z1’ and ‘z2’ for low and high redshift bins, respectively. The thresholds of the redshift and mass proxy are listed in the 3rd and 4th columns. The last column exhibits the total number of halos included. The last column lists the total halo number in the specific parameter range, with halos located outside of DECaLS DR8 coverage also included.

The performance of the final catalog ([Zou et al. 2019](#)) includes the redshift bias of $\Delta z_{\text{norm}} = 2.4 \times 10^{-4}$, accuracy of $\sigma_{\Delta z_{\text{norm}}} = 0.017$, and outlier rate of $\sim 5.1\%$.

2.2. Lens catalogs

Halos from five catalogs are used as lenses, including the redMaPPer (‘RM’ for short, [Rykoff et al. 2014](#)), ZOU21 ([Zou et al. 2021](#)), YANG21 ([Yang et al. 2021](#)), CMASS ([Ahn et al. 2014](#)), and LOWZ ([Ahn et al. 2014](#)) catalogs. To constrain the effects of redshift and halo mass, we divide each halo catalog into multiple bins, as shown in Fig. 1 and Tab. 1. To accurately characterize the entire sample and avoid bias from outliers in the redshift and mass parameter space, we discard halos outside of listed parameter ranges. The mass proxy used is the richness for redMaPPer catalog, the logarithm of M_{500} for ZOU21 catalog, the logarithm of halo mass for YANG21 catalog, and the logarithm of stellar mass for CMASS and LOWZ catalogs.

We use the 26,111 redMaPPer clusters (catalog v6.3¹) derived from the SDSS DR8 ([Rykoff et al. 2014](#)) as the lens catalog. The richness of these clusters are $\lambda > 19$. In each cluster, we take the galaxy with the highest center likelihood as the halo center. For an accurate center

¹ <http://risa.stanford.edu/redmapper/>

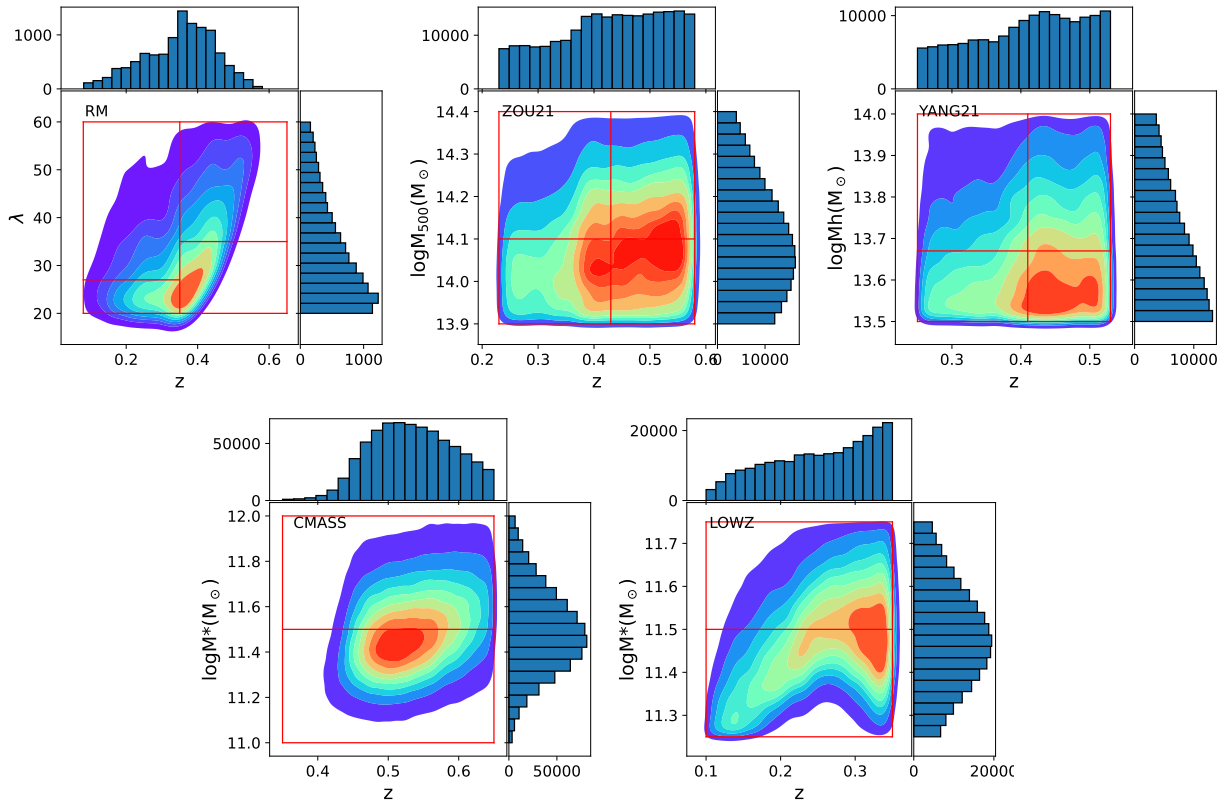


Figure 1. The bin criteria of lens catalogs in the redshift and mass proxy parameter space. From top to bottom, from left to right, the panels correspond to redMaPPer, ZOU21, YANG21, CMASS, and LOWZ catalog, in sequence. In each panel, the main plot illustrates the halo distribution in the redshift-mass space, with color representing halo number density. Redshift and mass proxy histograms are displayed in small plots above and to the right. Red horizontal and vertical lines indicate mass proxy and redshift thresholds. Galaxy clusters and groups beyond the labeled ranges are taken as outliers, and excluded from plots.

determination, we only use clusters exhibiting high centering probabilities ($P_{\text{cen}} > 0.95$). To understand the relation between the splashback radius and other parameters, such as redshift and mass, the redMaPPer cluster sample is divided into four bins, with high/low redshift and richness.

We divide redMaPPer clusters into high redshift and low redshift subsamples. Then, each subsample is separated into the less massive and more massive cluster bins. The redMaPPer halo bins are shown in the upper-left panel of Fig. 1. Using the galaxy-galaxy lensing measurements, we obtain the surface density profiles of clusters with different halo mass and redshift. With similar halo numbers in each bin, we control potential biases from the sample size in the signal measurement.

In addition, we use the halo catalogs of ZOU21 (Zou et al. 2021) and YANG21 (Yang et al. 2021). They identified 540, 432 galaxy clusters and 6.4 million galaxy groups from the DESI legacy imaging surveys (the Legacy Surveys) with a fast clustering algorithm and luminosity function, respectively. For the ZOU21 catalog, the density peak is taken as the halo center. For

the YANG21 catalog, we use the group catalog obtained from the DESI Image Legacy Surveys DR9 data² and take the position of the most massive member galaxy as the halo center. For reliability, we only use YANG21 groups with richness > 5 . Both ZOU21 and YANG21 catalogs are divided into four bins, for less massive and more massive halos at low redshift and high redshift. The distributions of halos are shown in the upper-middle and upper-right panel of Fig. 1.

Besides, we also utilize the CMASS and LOWZ catalogs from SDSS-III BOSS DR10 (Ahn et al. 2014) to constrain the splashback radius at low mass regions. The redshifts of CMASS and LOWZ halos are constrained within $0.35 - 0.65$ and $0.10 - 0.35$, respectively. For these two catalogs, we take the stellar mass as the halo mass proxy and separate each catalog into two mass bins, with the distributions shown in the second row of Fig. 1.

3. METHOD

² <https://gax.sjtu.edu.cn/data/DESI.html>

Table 2. Setting of *SWOT* parameters

Par.	Value	Meaning
corr	gglens	Type of correlation
range	0.1-30 Mpc/h	Correlation range
nbins	30	Number of bins
err	Jackknife	Resampling method
nsub	64	Number of resampling subvolumes
H ₀	67.4	Hubble parameter
Ω _m	0.315	Relative matter density
Ω _L	0.684	Relative energy density
Δ	0.1	Minimum redshift difference between the source and the lens
proj	como	Projection

Note. The parameter name, value, and corresponding physical meaning are presented in columns.

3.1. Measurement of galaxy-galaxy lensing signal

The projected mass density of the lens, Σ , is known related to the azimuthally averaged tangential shear at projected radius R . However, the differential surface density, $\Delta\Sigma(R)$, is usually used for the measurement of weak lensing signal, which is defined as

$$\Delta\Sigma = \bar{\Sigma}(< R) - \Sigma(R). \quad (1)$$

We use the *SWOT*³ software (Coupon et al. 2012) to measure the weak lensing signal for every halo bin, as shown in Fig. 2. The parameter setting is listed in Tab. 2.

The differential surface density is estimated as

$$\Delta\Sigma(R) = \frac{\sum_{\text{ls}} w_{\text{ls}} \gamma_t^{\text{ls}} \Sigma_{\text{crit}}}{\sum_{\text{ls}} w_{\text{ls}}}, \quad (2)$$

where γ_t^{ls} is the tangential shear, $w_{\text{ls}} = w_{\text{n}} \Sigma_{\text{crit}}^{-2}$, and w_{n} is the weight factor to account for intrinsic scatter in ellipticity and the error of shape measurement (Miller et al. 2007, 2013). The w_{n} used in this work is defined as $w_{\text{n}} = 1/(\sigma_{\epsilon}^2 + \sigma_e^2)$. The σ_{ϵ} is the intrinsic ellipticity dispersion derived from the whole galaxy sample, and taken as 0.27 (Giblin et al. 2021). σ_e is the error of the ellipticity measurement (Hoekstra et al. 2002).

The lensing signal is recalibrated as

$$\Delta\Sigma^{\text{cal}}(R) = \frac{\Delta\Sigma(R)}{1 + K(z_1)}, \quad (3)$$

and

$$1 + K(z_1) = \frac{\sum_{\text{ls}} w_{\text{ls}} (1 + m)}{\sum_{\text{ls}} w_{\text{ls}}}, \quad (4)$$

where m is the multiplicative error.

In the measurement of galaxy-galaxy lensing signal, there are multiple potential systematics. Potential uncertainties may arise due to the shear additive and multiplicative bias, the intrinsic alignments, the boost factor, and photo- z dilution. Firstly, the shear additive bias, which is expected from the residual of the shape fitting from anisotropic point spread function correction (Zuntz et al. 2018; McClintock et al. 2019), brings only negligible bias to our measurement of galaxy-galaxy lensing signal. We cross-match DECaLS sources with external shear measurements (Phriksee et al. 2020; Yao et al. 2020; Zu et al. 2021), including Canada-France-Hawaii Telescope Stripe 82 (Moraes et al. 2014), Dark Energy Survey (Dark Energy Survey Collaboration et al. 2016), and Kilo-Degree Survey (Hildebrandt et al. 2017) sources. This way, we obtain the multiplicative and additive biases. After correction, we expect the residual multiplicative bias of DECaLS DR8 shear catalog is $m \sim 5\%$ (Yao et al. 2020; Phriksee et al. 2020), possibly from the selection of observation data (Li et al. 2021; Jarvis et al. 2016) (i.e. the matched galaxies are not an exact representation of the full observational sample in terms of magnitude, color, size, etc.), or the slight differences between simulated galaxies and observations.

Furthermore, we only use bright galaxies with r -band magnitude < 23 as sources (Zou et al. 2019) to avoid photo- z outliers and keep the overlap between lens and sources at a very small level. In this case, both effects from intrinsic alignment (Yao et al. 2023a,b), and the one from boost factor are negligible (Melchior et al. 2017; McClintock et al. 2019). For the photo- z dilution (Lange et al. 2021), we have not made the $n(z)$ correction. Nevertheless, this is a scale-independent problem, similar to the residual shear multiplicative bias, which does not affect our splashback radius measurement.

3.2. Fitting of galaxy-galaxy lensing signal

In our measurement, the contribution of $\Delta\Sigma$ includes the central dark matter halo, the miscentering effect (Johnston et al. 2007), and nearby halos. To avoid the central region where the contribution from the central galaxy dominates, we only consider the signal within the radius range of 0.3 – 30 Mpc/h in the fitting. Thus, the whole model used is

$$\Delta\Sigma(R) = (1 - f_{\text{mis}}) \Delta\Sigma_{\text{ein}}(R) + f_{\text{mis}} \Delta\Sigma_{\text{mis}}(R|R_{\text{mis}}) + \Delta\Sigma_{\text{outer}}(R). \quad (5)$$

We use the Einasto profile (Einasto 1965) for the contribution of the central dark matter halo. Compared with the Navarro-Frenk-White profile (NFW profile, Navarro et al. 1996), the Einasto profile can characterize the dark matter halo profile more accurately

³ <http://jeancoupon.com/swot>

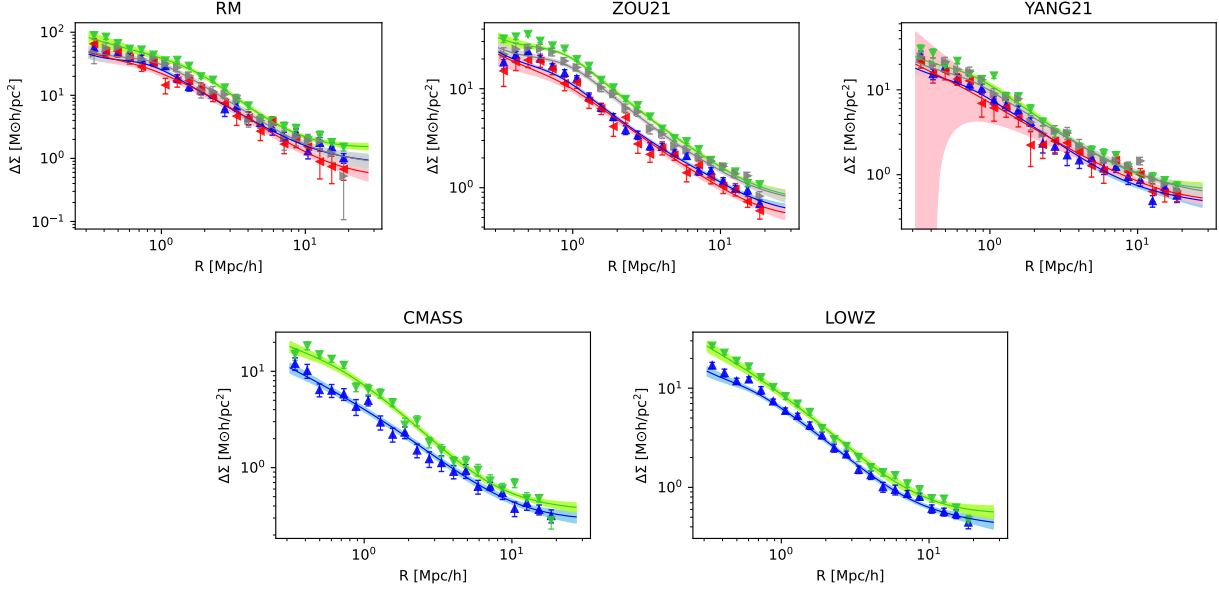


Figure 2. The measured stacked weak lensing signal for bins of catalogs, overlaid with the best fitting model. In the first row, the signal from the redMaPPer, ZOU21, and YANG21 catalogs are shown from left to right. In these three panels, the signals from the low- z low- M , low- z high- M , high- z low- M , and high- z high- M are shown in blue, green, red, and grey, respectively. In the second row, the signals from CMASS and LOWZ catalogs are shown in the left panel and the right panel. In these two panels, the low- M and high- M bins are shown in blue and green, respectively. For each bin, the best-fitting model is shown in the same color, together with a lighter shade region for its 1σ error range.

(Navarro et al. 2004, 2010; Gao et al. 2008; Ludlow et al. 2011).

The miscentering effect comes from the inaccurate determination of the halo center (Johnston et al. 2007), which greatly reduces the stacked signal at the central region. For a cluster offset from the cluster center by the distance of R_{mis} , its surface mass density becomes $\Sigma_{\text{mis}} = \int_0^{2\pi} d\theta \Sigma(\sqrt{R^2 + R_{\text{mis}}^2 + 2RR_{\text{mis}}\cos\theta})/2\pi$. The Gamma profile is assumed to obtain the miscentering signal of the stacked signal (McClintock et al. 2019). f_{mis} and R_{mis} are the two characteristic parameters, for the fraction of offset halos and the offset distance, respectively.

The last term in Eq. 5 is the outer term indicating the signal from nearby halos, which dominates at the cluster outskirts. This term is estimated from the non-linear scaling of the matter power spectrum as a function of redshift with the *Halofit* model using the *CAMB* package⁴ (Lewis & Bridle 2002; Lewis et al. 2000; Howlett et al. 2012).

3.3. Estimation of splashback radius

For estimation of the splashback radius, we need to obtain the profile of the halo density. In this work, we use the density profile from Diemer & Kravtsov (2014)

(DK14 profile for short):

$$\begin{aligned}
 \rho(r) &= \rho_{\text{inner}} \times f_{\text{trans}} + \rho_{\text{outer}}, \\
 \rho_{\text{inner}} &= \rho_{\text{Einasto}} = \rho_s \exp\left(-\frac{2}{\alpha}\left[\left(\frac{r}{r_s}\right)^\alpha - 1\right]\right), \\
 f_{\text{trans}} &= \left[1 + \left(\frac{r}{r_t}\right)^\beta\right]^{-\frac{\gamma}{\beta}}, \\
 \rho_{\text{outer}} &= \frac{\text{Norm}}{\left(\frac{r}{5R_{200m}}\right)^{\text{slope}} + 1}.
 \end{aligned} \tag{6}$$

The DK14 profile exhibits an Einasto profile in its inner region, transitioning to a steeper gradient near the virial radius. The Einasto profile incorporates six free parameters: ρ_s , representing the density at the scale radius; r_s , the scale radius; r_t , the truncation radius where the profile steepens beyond the Einasto profile; α , a factor determining the rate at which the slope of the inner Einasto profile increases; β , the sharpness of the steepening; γ , the asymptotic negative incline of the steepening term. Besides, the normalization and slope from the outer term are also free parameters. Furthermore, the distance and fraction of the miscentering are other free parameters. We use the *Colossus* software⁵ (Diemer 2018), and the *Cluster_toolkit* software⁶ (Mc-

⁴ <https://github.com/cmbant/CAMB>

⁵ <https://bdiemer.bitbucket.io/colossus/>

⁶ <https://cluster-toolkit.readthedocs.io/en/latest/index.html>

Table 3. Prior ranges of parameters.

Par.	Prior value	Min.	Max.
ρ_s [$10^{12}M_\odot h^2/\text{Mpc}^3$]	10	0.1	1,000
r_s [Mpc/h]	0.40	0.10	1.50
r_t [Mpc/h]	1.84	1.00	6.00
$\log(\alpha)$	[$\log(0.22)$, 0.6]	$\log(0.01)$	$\log(10)$
$\log(\beta)$	[$\log(6)$, 0.2]	$\log(0.01)$	$\log(30)$
$\log(\gamma)$	[$\log(4)$, 0.2]	$\log(0.01)$	$\log(30)$
Norm	300	50	3,000
slope	0.9	0.1	0.99
R_{mis} [Mpc/h]	0.55	0.0	1.0
f_{mis}	0.2	0.0	1.0

Note. The prior value, minimum, and maximum values of parameters are presented in columns. The α , β , and γ are logarithm Gaussian distributed, with the mean and full width at half maximum (FWHM) shown in the *Prior value* column. The prior settings for α , β , and γ are based on Shin et al. (2019, 2021); Adhikari et al. (2021); Dacunha et al. (2022).

Clintock et al. 2019) to model the density profile and the corresponding surface density profile.

We make the model-fitting using the Markov Chain Monte Carlo (MCMC) technique (*EMCEE* package⁷, Foreman-Mackey et al. 2013a). The number of chains is 50, with 6,000 steps each. The priors are set according to Tab. 3, with the starting value of each chain exhibiting a variation of 0.1% around the specified value. To minimize the bias originating from priors, we discard the initial 3,000 steps. One parameter set is retained for every three sets.

By deriving the best-fit density profile for the given cluster sample, we obtain the MCMC chain which describes the posterior distribution of our model parameters for the density profile. Then we calculate the $d\log(\rho)/d\log(r)$ for each point within the MCMC chain. Utilizing the equation sets outlined in Eq. 6, we derive R_{sp} as the radius with the minimum value of the density slope, $d\log\rho(r)/d\log r$.

This way, we obtain the posterior distribution of R_{sp} . Subsequently, we determine the best fit R_{sp} by averaging the posterior parameter space, and its associated uncertainty is given by calculating the confidence level 68% of the posterior distribution.

The modeling of the infalling term does not affect the best-fit R_{sp} in our measurement. In the model, the contribution from the infalling material is modeled as the

power-law term. And the splashback radius is still notable in the profile of the density slope.

4. RESULT AND DISCUSSION

4.1. Measurement of the splashback radius

The fitting results for the low redshift, high mass bin of redMaPPer clusters are illustrated in Fig. 3 as an example. The figure comprises four panels, presenting the galaxy-galaxy lensing signal with the best-fitting model and its model components, the differential surface density multiplied by the radius, the density slope, and the density profile. In the lower-left panel, for each set of parameters in the MCMC chains, a profile of the density slope is obtained, and the best-fit model and its 1σ range are estimated at each radius. On the other hand, the best-fitting splashback radius and its 1σ range are calculated as the minimum location of each profile. As a result, the value of splashback radius and its 1σ range does not necessarily match with the bottom range of the distribution of the $d\log(\rho)/d\log(r)$.

The values of the optimal fitting parameters are listed on Tab. 4. Notably, the reasonable reduced- χ^2 values of the best fitting in the last column indicate that our model effectively characterizes the features of the galaxy-galaxy lensing signal.

In addition to our measurements, we have compiled a list of splashback radius measurements from the literature. These are presented in the first part of Tab. 5, with our results in the second part for comparison. The sample listed in Tab. 5, including both literature results and our measurements, is named as “the whole sample” in later text. These literature works make measurements mainly using weak lensing signal and galaxy number density profiles, for various cluster catalogs, including DES redMaPPer (Chang et al. 2018; Shin et al. 2019), HSC redMaPPer (Murata et al. 2020), X-ray clusters (Contigiani et al. 2019; Bianconi et al. 2021), SZ-selected clusters (Shin et al. 2019; Zürcher & More 2019; Adhikari et al. 2021; Shin et al. 2021), and luminous red galaxies from KiDS (Contigiani et al. 2023).

In compiling literature works, we have standardized the values to the same unit and accounted for differences in the Hubble constant. When both the values of R_{sp} and $R_{\text{sp}}/R_{200\text{m}}$ are provided, we calculate the $R_{200\text{m}}$ values from them; otherwise, the $R_{200\text{m}}$ value is calculated from $M_{200\text{m}}$ and the redshift. The corresponding errors are propagated as Eq. 7. The concentration value listed in Tab. 5 is one of the fitting parameters in our model. It is converted to the value at $z = 0$ by multiplying $(1+z)^{0.67}$ (Klypin et al. 2016).

⁷ <https://emcee.readthedocs.io/en/stable/>

Table 4. The optimal parameter fitting results.

Cat.	bin	ρ_s	r_s	r_t	$\log(\alpha)$	$\log(\beta)$	$\log(\gamma)$	Norm	Slope	R_{mis}	f_{mis}	χ^2/ν
(1)	(2)	(3)	(4)	(5)	(6)	(7)	(8)	(9)	(10)	(11)	(12)	(13)
RM	z1m1	14.20 ^{+12.71} _{-8.21}	0.62 ^{+0.35} _{-0.20}	3.68 ^{+1.57} _{-1.48}	-0.89 ^{+0.41} _{-0.50}	0.77 ^{+0.20} _{-0.22}	0.57 ^{+0.19} _{-0.19}	342 ⁺²¹⁴ ₋₁₈₈	0.89 ^{+0.07} _{-0.11}	0.33 ^{+0.02} _{-0.02}	0.57 ^{+0.18} _{-0.22}	1.60
RM	z1m2	33.54 ^{+23.29} _{-13.08}	0.58 ^{+0.20} _{-0.15}	1.47 ^{+1.07} _{-0.34}	-1.08 ^{+0.97} _{-0.39}	0.73 ^{+0.22} _{-0.24}	0.67 ^{+0.20} _{-0.18}	712 ⁺⁴²⁷ ₋₄₅₂	0.89 ^{+0.07} _{-0.15}	0.46 ^{+0.30} _{-0.19}	0.16 ^{+0.13} _{-0.10}	2.78
RM	z2m1	17.57 ^{+26.07} _{-10.76}	0.55 ^{+0.35} _{-0.21}	2.75 ^{+1.70} _{-1.28}	-0.97 ^{+0.56} _{-0.54}	0.74 ^{+0.22} _{-0.23}	0.59 ^{+0.21} _{-0.20}	141 ⁺¹²⁶ ₋₆₅	0.91 ^{+0.06} _{-0.10}	0.31 ^{+0.21} _{-0.05}	0.26 ^{+0.21} _{-0.18}	1.56
RM	z2m2	40.03 ^{+57.44} _{-29.87}	0.42 ^{+0.46} _{-0.15}	3.08 ^{+1.94} _{-1.55}	-0.72 ^{+0.40} _{-0.60}	0.74 ^{+0.22} _{-0.20}	0.62 ^{+0.19} _{-0.19}	211 ⁺¹⁹⁹ ₋₁₁₃	0.91 ^{+0.06} _{-0.12}	0.39 ^{+0.09} _{-0.05}	0.50 ^{+0.26} _{-0.30}	1.28
ZOU21	z1m1	10.20 ^{+12.77} _{-5.21}	0.45 ^{+0.20} _{-0.16}	5.23 ^{+0.55} _{-0.91}	-1.43 ^{+0.30} _{-0.31}	0.90 ^{+0.16} _{-0.17}	0.57 ^{+0.20} _{-0.19}	221 ⁺¹⁰⁸ ₋₉₅	0.92 ^{+0.05} _{-0.09}	0.31 ^{+0.02} _{-0.02}	0.38 ^{+0.09} _{-0.09}	4.19
ZOU21	z1m2	11.13 ^{+7.37} _{-4.51}	0.62 ^{+0.21} _{-0.15}	5.10 ^{+0.62} _{-0.92}	-0.89 ^{+0.19} _{-0.24}	0.84 ^{+0.19} _{-0.20}	0.55 ^{+0.19} _{-0.20}	321 ⁺¹²⁷ ₋₁₄₃	0.93 ^{+0.05} _{-0.09}	0.36 ^{+0.02} _{-0.02}	0.52 ^{+0.07} _{-0.10}	2.26
ZOU21	z2m1	25.35 ^{+24.34} _{-15.51}	0.28 ^{+0.17} _{-0.08}	4.85 ^{+0.82} _{-1.12}	-1.12 ^{+0.33} _{-0.39}	0.82 ^{+0.19} _{-0.21}	0.59 ^{+0.18} _{-0.18}	139 ⁺⁹⁷ ₋₆₅	0.92 ^{+0.05} _{-0.09}	0.34 ^{+0.29} _{-0.05}	0.21 ^{+0.26} _{-0.16}	2.09
ZOU21	z2m2	12.50 ^{+10.73} _{-6.77}	0.53 ^{+0.27} _{-0.15}	4.95 ^{+0.77} _{-1.33}	-0.99 ^{+0.34} _{-0.42}	0.84 ^{+0.18} _{-0.23}	0.55 ^{+0.19} _{-0.19}	204 ⁺¹¹⁸ ₋₉₈	0.93 ^{+0.05} _{-0.10}	0.37 ^{+0.03} _{-0.03}	0.54 ^{+0.11} _{-0.19}	2.39
YANG21	z1m1	12.12 ^{+10.13} _{-6.53}	0.35 ^{+0.15} _{-0.09}	2.94 ^{+2.07} _{-1.65}	-0.76 ^{+0.46} _{-0.49}	0.75 ^{+0.23} _{-0.29}	0.59 ^{+0.20} _{-0.21}	151 ⁺¹⁴⁵ ₋₇₇	0.92 ^{+0.05} _{-0.09}	0.25 ^{+0.06} _{-0.04}	0.41 ^{+0.29} _{-0.27}	3.08
YANG21	z1m2	12.89 ^{+9.79} _{-6.49}	0.42 ^{+0.18} _{-0.12}	3.50 ^{+1.76} _{-2.15}	-0.92 ^{+0.32} _{-0.37}	0.72 ^{+0.23} _{-0.35}	0.60 ^{+0.21} _{-0.22}	252 ⁺¹⁴⁵ ₋₁₂₀	0.92 ^{+0.05} _{-0.10}	0.29 ^{+0.40} _{-0.02}	0.41 ^{+0.29} _{-0.28}	4.01
YANG21	z2m1	15.06 ^{+29.91} _{-9.74}	0.28 ^{+0.20} _{-0.11}	4.58 ^{+0.97} _{-1.68}	-1.18 ^{+0.46} _{-0.42}	0.76 ^{+0.19} _{-0.18}	0.61 ^{+0.19} _{-0.22}	149 ⁺⁹⁷ ₋₆₇	0.93 ^{+0.05} _{-0.08}	0.22 ^{+0.15} _{-0.10}	0.22 ^{+0.36} _{-0.17}	1.27
YANG21	z2m2	11.91 ^{+14.80} _{-7.04}	0.39 ^{+0.24} _{-0.12}	4.63 ^{+0.97} _{-1.76}	-1.02 ^{+0.44} _{-0.47}	0.80 ^{+0.20} _{-0.21}	0.56 ^{+0.20} _{-0.18}	161 ⁺¹⁰⁴ ₋₇₅	0.92 ^{+0.05} _{-0.10}	0.28 ^{+0.03} _{-0.03}	0.43 ^{+0.32} _{-0.26}	1.83
CMASS	m1	31.11 ^{+24.23} _{-19.41}	0.16 ^{+0.11} _{-0.04}	3.89 ^{+1.37} _{-1.99}	-0.97 ^{+0.28} _{-0.23}	0.76 ^{+0.21} _{-0.23}	0.64 ^{+0.24} _{-0.22}	95 ⁺⁵² ₋₂₇	0.94 ^{+0.04} _{-0.06}	0.32 ^{+0.51} _{-0.21}	0.08 ^{+0.12} _{-0.06}	1.34
CMASS	m2	38.44 ^{+35.19} _{-23.48}	0.20 ^{+0.10} _{-0.04}	3.53 ^{+1.61} _{-2.13}	-0.53 ^{+0.23} _{-0.30}	0.75 ^{+0.20} _{-0.25}	0.60 ^{+0.21} _{-0.20}	122 ⁺⁵² ₋₅₅	0.94 ^{+0.04} _{-0.08}	0.26 ^{+0.44} _{-0.06}	0.15 ^{+0.15} _{-0.12}	3.30
LOWZ	m1	13.39 ^{+9.46} _{-6.38}	0.30 ^{+0.12} _{-0.06}	3.44 ^{+1.75} _{-1.99}	-0.71 ^{+0.29} _{-0.40}	0.73 ^{+0.23} _{-0.21}	0.59 ^{+0.19} _{-0.21}	232 ⁺¹³⁴ ₋₁₁₆	0.93 ^{+0.04} _{-0.06}	0.25 ^{+0.04} _{-0.03}	0.27 ^{+0.22} _{-0.19}	1.66
LOWZ	m2	15.97 ^{+8.70} _{-5.52}	0.39 ^{+0.09} _{-0.09}	2.05 ^{+1.83} _{-0.81}	-1.38 ^{+0.41} _{-0.31}	0.21 ^{+0.36} _{-0.17}	0.46 ^{+0.25} _{-0.22}	397 ⁺¹¹⁹ ₋₁₆₇	0.95 ^{+0.03} _{-0.07}	0.41 ^{+0.53} _{-0.19}	0.06 ^{+0.14} _{-0.05}	4.56

Note: The first two columns show the catalog name and bin names, while the subsequent ten columns present the parameters for the fitting of differential surface density profile, $\Delta\Sigma(R)$, in Eq. 5 and Eq. 6. The last column denotes the reduced χ^2 for the best fit. The unit of ρ_s is $10^{12}M_\odot h^2/\text{Mpc}^3$. The r_s , r_t , and R_{mis} are all in the unit of Mpc/h . All listed errors correspond to the 1σ range.

$$\begin{aligned}
(\sigma_z/z) &= a * (\sigma_x/x), & (z = x^a) \\
(\sigma_z/z)^2 &= (\sigma_x/x)^2 + (\sigma_y/y)^2, & (z = x * y) \\
(\sigma_z/z)^2 &= (\sigma_x/x)^2 + (\sigma_y/y)^2, & (z = x/y)
\end{aligned} \quad (7)$$

4.2. Dependence of R_{sp} on halo mass, redshift, and $R_{200\text{m}}$

We investigate the density slope profiles and the associated splashback radii for each catalog bin to gain an insight into the factors that influence the splashback radius (see Fig. 4). Our findings demonstrate a general positive correlation between splashback radius and the mass of the clusters, while there appears to be no dependence of splashback radius on redshift.

In Fig. 5, the relation between halo mass and the splashback radius or the normalized splashback radius is plotted in 4 redshift bins, with redshift represented by the color of data points. The sample size of each redshift bin is roughly equal. In each redshift bin, there exists a positive tendency between the splashback radius and halo mass remains, especially in the lowest redshift bin. However, this correlation between them becomes much weaker when the splashback radius is normalized. And the relation shows a U-shape, especially in the two lowest redshift bins. However, the measurement uncertainty is too large for a robust conclusion.

In the left panel of Fig. 6, we illustrate the correlation between halo mass and the splashback radius for

the whole sample across the whole redshift range. The positive correlation between the splashback radius and halo mass remains. Additionally, we depict the relation between the normalized splashback radius and the halo mass in the right panel therein. The U-shaped trend is distinctive, with a pivot point around $10^{14}M_\odot$. However, the upturns in both relations are likely caused by massive halos with low redshifts, because low redshift halos correspond to a lower peak height than high redshift halos with the same mass. In both plots, there is no clear observable correlation between the splashback radius and redshift at a given halo mass. Notably, our measurements align consistently with literature results within a 1σ range.

4.3. The relationship between the splashback radius and peak height

Theoretically, the peak height of the halo influences the accretion rate and the radial motion of the accreted matter, thus it also impacts the splashback radius. We explore the relation between the peak height and the splashback radius. Following More et al. (2015), we calculate peak height as

$$\nu = \nu_{200\text{m}} \equiv \delta_c / \sigma(M_{200\text{m}}) / D(z), \quad (8)$$

where δ_c denotes the critical threshold at which the collapse begins, σ^2 is the fluctuation variance of the initial density map, and $D(z)$ is the growth factor.

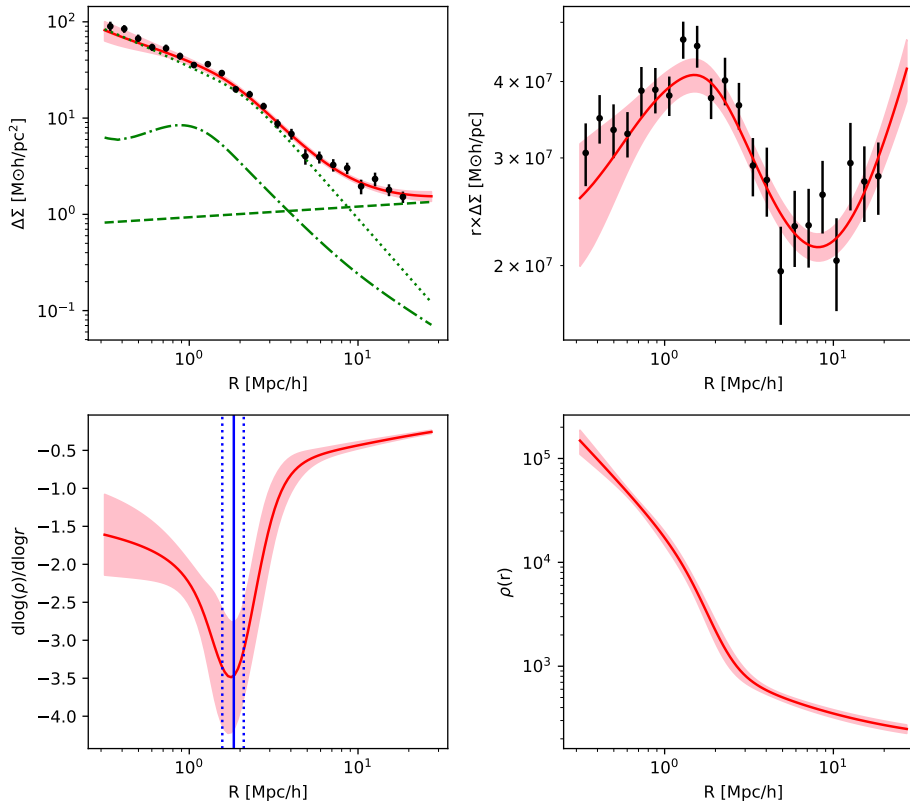


Figure 3. The panels show the profile of the differential surface density ($\Delta\Sigma(R)$), $r \times \Delta\Sigma(R)$, the density slope, and the density for the fitting result of redMaPPer halos in the low-redshift high-mass bins. The data points with error bars are represented by black dots, while the optimal model and its 1σ range are represented by a red curve and pink shading, respectively. In the upper-left panel, the contributions from the central halo, miscentering effect, and nearby halo are overlaid as dotted, dot-dashed, and dashed green curves. In the lower-left panel, the best-fit splashback radius and its 1σ range are displayed as the solid blue vertical line and dotted blue vertical lines.

In Fig. 7, we depict the relationship between the peak height and the normalized splashback radius. We find the splashback radius increases with the peak height, although the scatters are large. However, this tendency is also highly affected by massive halos at low redshifts, whose sizes are large in the case of virial radius. Thus, the normalized splashback radius is also depicted for its relation with halo mass in this Figure. We find the upturn of splashback radius for massive halos has been greatly reduced after it is normalized. In both panels, our measurements are aligned with literature in $\sim 1\sigma$ range. Furthermore, the binned data of the whole sample are compared with the parameterized function from the simulation work of More et al. (2015), as

$$R_{\text{sp}}/R_{200\text{m}} = A (1 + B e^{-\nu/C}). \quad (9)$$

In the work of More et al. (2015), the parameters in Eq. 9 are estimated as $A = 0.81$, $B = 0.97$, $C = 2.44$. However, we find the measurements deviated from the model using these parameter values. The reduced χ^2 for the binned data of the whole sample is 6.73.

We fit the binned data of the whole sample with the Eq. 9 and obtain the best-fit parameters as $A = 1.20^{+0.22}_{-0.64}$, $B = 0.66^{+2.91}_{-1.17}$, $C = 3.03^{+5.08}_{-2.74}$. The best-fitting model is overlaid in Fig. 7. We find the best-fitting model is consistent with the model of More et al. (2015), although the normalization has some offset mightly due to systematics, such as different fitting procedures (O’Neil et al. 2021).

In Diemer & Kravtsov (2014), the relation between the accretion rate and the normalized splashback radius is

$$R_{\text{sp}}/R_{200\text{m}} = 0.54 [1 + 0.53\Omega_{\text{m}}(z)] (1 + 1.36 e^{-\Gamma/3.04}), \quad (10)$$

where the Γ is the accretion rate. The normalized splashback found in the simulation has a negative correlation with the accretion rate (Diemer & Kravtsov 2014; Diemer et al. 2017). It is the result of the shrinking apocenter of accreted matter in the rapidly growing potential well.

Specifically, More et al. (2015) constrain the splashback radius from halo merger trees from numerical simu-

Table 5. Splashback radius measurements in the “whole sample”, including literature and our work.

Index (1)	Mean M_{200m} (2)	z (3)	R_{sp} [Mpc/h] (4)	R_{200m} [Mpc/h] (5)	R_{sp}/R_{200m} (6)	$c(z=0)$ (7)	Sample (8)	Measurement (9)
1	$1.69^{+0.31}_{-0.31}$	0.41	$1.13^{+0.07}_{-0.07}$	$0.78^{+0.05}_{-0.05}$	$0.82^{+0.05}_{-0.05}$	-	DES RM	G profile
2	$1.69^{+0.79}_{-0.79}$	0.41	$1.34^{+0.21}_{-0.21}$	$0.78^{+0.12}_{-0.12}$	$0.97^{+0.15}_{-0.15}$	-	DES RM	WL
3	$1.71^{+0.08}_{-0.07}$	0.57	$1.50^{+0.19}_{-0.18}$	$1.32^{+0.02}_{-0.02}$	$1.14^{+0.14}_{-0.14}$	-	HSC RM	G profile
4	$11.46^{+10.78}_{-6.85}$	0.28	$2.36^{+0.74}_{-0.47}$	$1.54^{+0.48}_{-0.31}$	$1.53^{+0.68}_{-0.43}$	-	CCCP X-ray	WL
5	$14.03^{+0.12}_{-0.12}$	0.23	$3.81^{+0.75}_{-0.75}$	$2.18^{+0.01}_{-0.01}$	$1.74^{+0.34}_{-0.34}$	-	LoCuss X-ray	G profile
6	$5.10^{+1.56}_{-1.34}$	0.46	$1.06^{+0.11}_{-0.09}$	$1.10^{+0.11}_{-0.10}$	$0.97^{+0.07}_{-0.06}$	-	DES RM	G profile
7	$5.10^{+4.61}_{-4.43}$	0.49	$1.32^{+0.40}_{-0.38}$	$1.08^{+0.33}_{-0.31}$	$1.22^{+0.26}_{-0.25}$	-	SPT SZ	G profile
8	$5.60^{+7.71}_{-5.99}$	0.49	$1.24^{+0.57}_{-0.44}$	$1.12^{+0.51}_{-0.40}$	$1.11^{+0.36}_{-0.28}$	-	ACT SZ	G profile
9	$5.87^{+2.47}_{-2.87}$	0.18	$1.78^{+0.25}_{-0.29}$	$1.28^{+0.18}_{-0.21}$	$1.39^{+0.28}_{-0.32}$	-	Planck SZ	G profile
10	$4.62^{+3.50}_{-4.90}$	0.46	$1.19^{+0.30}_{-0.42}$	$1.06^{+0.27}_{-0.38}$	$1.12^{+0.20}_{-0.28}$	-	ACT SZ	WL
11	$4.62^{+1.11}_{-2.40}$	0.46	$1.13^{+0.09}_{-0.20}$	$1.06^{+0.09}_{-0.18}$	$1.06^{+0.06}_{-0.13}$	-	ACT SZ	G profile
12	$5.77^{+2.17}_{-2.90}$	0.49	$2.39^{+0.30}_{-0.40}$	$1.13^{+0.14}_{-0.19}$	$2.11^{+0.38}_{-0.50}$	-	ACT DR5 SZ	G profiles
13	$0.38^{+0.24}_{-0.14}$	0.44	$1.00^{+0.13}_{-0.13}$	$0.47^{+0.06}_{-0.06}$	$2.15^{+0.39}_{-0.39}$	-	KiDS	Splash-back
14	$3.38^{+0.82}_{-0.82}$	$0.2620^{+0.0671}_{-0.0670}$	$1.96^{+1.05}_{-1.05}$	$1.03^{+0.08}_{-0.08}$	$1.90^{+1.03}_{-1.03}$	$4.95^{+1.62}_{-1.62}$	RM,z1m1	WL
15	$9.10^{+2.54}_{-2.54}$	$0.2564^{+0.0682}_{-0.0682}$	$1.84^{+0.27}_{-0.27}$	$1.44^{+0.13}_{-0.13}$	$1.27^{+0.22}_{-0.22}$	$7.46^{+2.00}_{-2.00}$	RM,z1m2	WL
16	$3.10^{+1.06}_{-1.06}$	$0.3962^{+0.0317}_{-0.0317}$	$2.04^{+0.79}_{-0.79}$	$0.95^{+0.11}_{-0.11}$	$2.14^{+0.86}_{-0.86}$	$5.83^{+2.55}_{-2.55}$	RM,z2m1	WL
17	$4.22^{+1.18}_{-1.18}$	$0.4472^{+0.0528}_{-0.0527}$	$2.06^{+0.85}_{-0.85}$	$1.04^{+0.10}_{-0.10}$	$1.98^{+0.84}_{-0.84}$	$7.71^{+3.40}_{-3.39}$	RM,z2m2	WL
18	$0.86^{+0.08}_{-0.08}$	$0.3403^{+0.0585}_{-0.0585}$	$0.44^{+0.17}_{-0.17}$	$0.63^{+0.02}_{-0.02}$	$0.69^{+0.27}_{-0.27}$	$4.63^{+1.57}_{-1.56}$	ZOU21,z1m1	WL
19	$2.52^{+0.35}_{-0.35}$	$0.3459^{+0.0579}_{-0.0578}$	$1.22^{+0.42}_{-0.42}$	$0.91^{+0.04}_{-0.04}$	$1.35^{+0.47}_{-0.47}$	$4.49^{+1.05}_{-1.05}$	ZOU21,z1m2	WL
20	$0.71^{+0.15}_{-0.15}$	$0.5040^{+0.0428}_{-0.0429}$	$0.60^{+0.25}_{-0.25}$	$0.56^{+0.04}_{-0.04}$	$1.08^{+0.45}_{-0.45}$	$6.52^{+2.27}_{-2.27}$	ZOU21,z2m1	WL
21	$1.62^{+0.21}_{-0.21}$	$0.5074^{+0.0433}_{-0.0434}$	$0.97^{+0.45}_{-0.45}$	$0.74^{+0.03}_{-0.03}$	$1.32^{+0.61}_{-0.61}$	$4.65^{+1.37}_{-1.37}$	ZOU21,z2m2	WL
22	$0.49^{+0.34}_{-0.34}$	$0.3365^{+0.0467}_{-0.0467}$	$0.94^{+0.36}_{-0.36}$	$0.53^{+0.12}_{-0.12}$	$1.78^{+0.79}_{-0.79}$	$4.51^{+1.36}_{-1.36}$	YANG21,z1m1	WL
23	$1.00^{+0.59}_{-0.59}$	$0.3367^{+0.0469}_{-0.0469}$	$0.94^{+0.40}_{-0.40}$	$0.67^{+0.13}_{-0.13}$	$1.41^{+0.66}_{-0.66}$	$4.71^{+1.31}_{-1.31}$	YANG21,z1m2	WL
24	$0.37^{+0.16}_{-0.16}$	$0.4694^{+0.0348}_{-0.0348}$	$0.51^{+0.26}_{-0.26}$	$0.45^{+0.06}_{-0.06}$	$1.11^{+0.59}_{-0.59}$	$5.58^{+2.61}_{-2.60}$	YANG21,z2m1	WL
25	$0.60^{+0.19}_{-0.19}$	$0.4707^{+0.0353}_{-0.0353}$	$0.70^{+0.39}_{-0.39}$	$0.54^{+0.06}_{-0.06}$	$1.31^{+0.74}_{-0.74}$	$4.64^{+1.75}_{-1.75}$	YANG21,z2m2	WL
26	$0.19^{+0.04}_{-0.04}$	$0.5219^{+0.0563}_{-0.0563}$	$0.58^{+0.32}_{-0.32}$	$0.35^{+0.03}_{-0.03}$	$1.62^{+0.92}_{-0.92}$	$6.78^{+2.36}_{-2.36}$	CMASS,m1	WL
27	$0.36^{+0.06}_{-0.06}$	$0.5467^{+0.0565}_{-0.0566}$	$0.89^{+0.25}_{-0.25}$	$0.44^{+0.03}_{-0.03}$	$2.04^{+0.58}_{-0.58}$	$7.21^{+2.19}_{-2.19}$	CMASS,m2	WL
28	$0.39^{+0.14}_{-0.14}$	$0.2379^{+0.0726}_{-0.0727}$	$0.88^{+0.30}_{-0.30}$	$0.51^{+0.06}_{-0.06}$	$1.72^{+0.62}_{-0.62}$	$4.77^{+1.22}_{-1.22}$	LOWZ,m1	WL
29	$1.17^{+0.47}_{-0.47}$	$0.2691^{+0.0565}_{-0.0564}$	$0.79^{+0.22}_{-0.22}$	$0.72^{+0.10}_{-0.10}$	$1.10^{+0.34}_{-0.34}$	$5.44^{+1.05}_{-1.05}$	LOWZ,m2	WL

The column is, in sequence, the index, halo mass, redshift, splashback radius, R_{200m} , normalized splashback radius, concentration at $z=0$, sample name, and measurement method. In the last column, WL is short for weak lensing method. The first 13 rows are obtained from literature, whose reference is as follows. 1, [Chang et al. \(2018\)](#); 2, [Chang et al. \(2018\)](#); 3, [Murata et al. \(2020\)](#); 4, [Contigiani et al. \(2019\)](#); 5, [Bianconi et al. \(2021\)](#); 6, [Shin et al. \(2019\)](#); 7, [Shin et al. \(2019\)](#); 8, [Shin et al. \(2019\)](#); 9, [Zürcher & More \(2019\)](#); 10, [Shin et al. \(2021\)](#); 11, [Shin et al. \(2021\)](#); 12, [Adhikari et al. \(2021\)](#); 13, [Contigiani et al. \(2023\)](#). The data listed in the 14th to 29th rows are the results of this work.

lations, and find R_{sp} is $0.8-1R_{200m}$ for halos with rapid accretion and is $\sim 1.5R_{200m}$ for halos with slow accretion. In the right panel of Fig. 7, we find the splashback radius is mostly $\gtrsim R_{200m}$ in the whole sample, meaning these halos tend to have a low accretion rate.

Furthermore, several other theoretical studies are exploring the dependence of the splashback radius on parameters such as mass accretion rate (Γ), height peak (ν), and redshift (z). Using a simple spherical collapse model of cosmological N-body halos, [Adhikari et al. \(2014\)](#) concluded that the normalized splashback radius (R_{sp}/R_{200m}) is smaller for halos with higher accretion

rates, where particle orbits contract within deep potential wells, particularly for halos located in low-redshift regions with low background density. This finding is supported by [Shi \(2016\)](#), who suggested that the correlation with redshift originates from a high Ω_m and the accretion rate at high redshift. Although [Diemer & Kravtsov \(2014\)](#) derived the normalized splashback radius from the density profiles of Λ CDM halos and found it to be small for halos with high accretion rates but with no redshift evolution, the recent works in [Diemer et al. \(2017\)](#); [Diemer \(2020\)](#) find some evidence of the redshift evolution of R_{sp} .

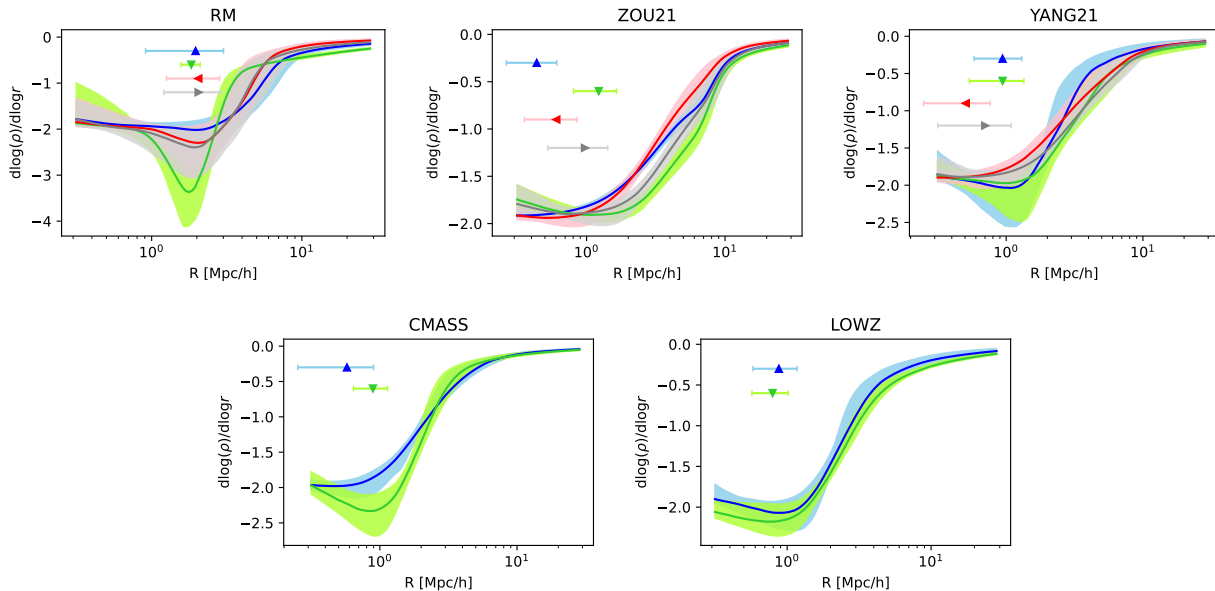


Figure 4. Profile of the density slope and corresponding value of splashback radius. The catalog name is shown at the top of each panel. The colors and symbols are consistent with Fig. 2. The solid curve and its corresponding light-colored shading represent the best-fit model and its 1σ range. The data point and horizontal error bar denote the best-fit splashback radius and its 1σ range. We use different Y values of the data points to separate the results of bins.

5. CONCLUSION

In this study, we measure and model the combined weak lensing signal for the redMaPPer, ZOU21, YANG21, CMASS, and LOWZ catalogs, which are divided into different redshift and mass. We employ a three-component model to fit $\Delta\Sigma(R)$, including contributions from the central halo, miscentering effect, and the external halo. The splashback radius for each bin is derived from the best-fit $\Delta\Sigma(R)$. We highlight the broad mass and redshift ranges over which we measure the splashback radius.

Our findings indicate a consistent increase in the splashback radius with halo mass across the entire mass range. However, the normalized splashback radius R_{sp}/R_{200} does not exhibit a monotonic growth with halo mass; instead, it displays a U-shaped trend, which might result from the redshift evolution. In addition, we find a positive relation of the splashback radius and a negative relation of the normalized splashback radius with the peak height, and the latter one is consistent with the prediction from More et al. (2015). Furthermore, in the whole sample, combining literature and our measurements, the splashback radius is mostly $\gtrsim R_{200\text{m}}$, meaning these halos tend to have a low accretion rate. However, the uncertainty in the measurements is very large. Future, more in-depth observations, and simulations are crucial for resolving this issue.

Software: Cluster toolkit (Smith et al. 2003; Eisenstein & Hu 1998; Takahashi et al. 2012), Colossus software (Diemer 2018), CAMB (Challinor & Lewis 2011; Lewis et al. 2000), SWOT (Coupon et al. 2012), EMCEE (Foreman-Mackey et al. 2013b), WebPlotDigitizer (Rohatgi 2020).

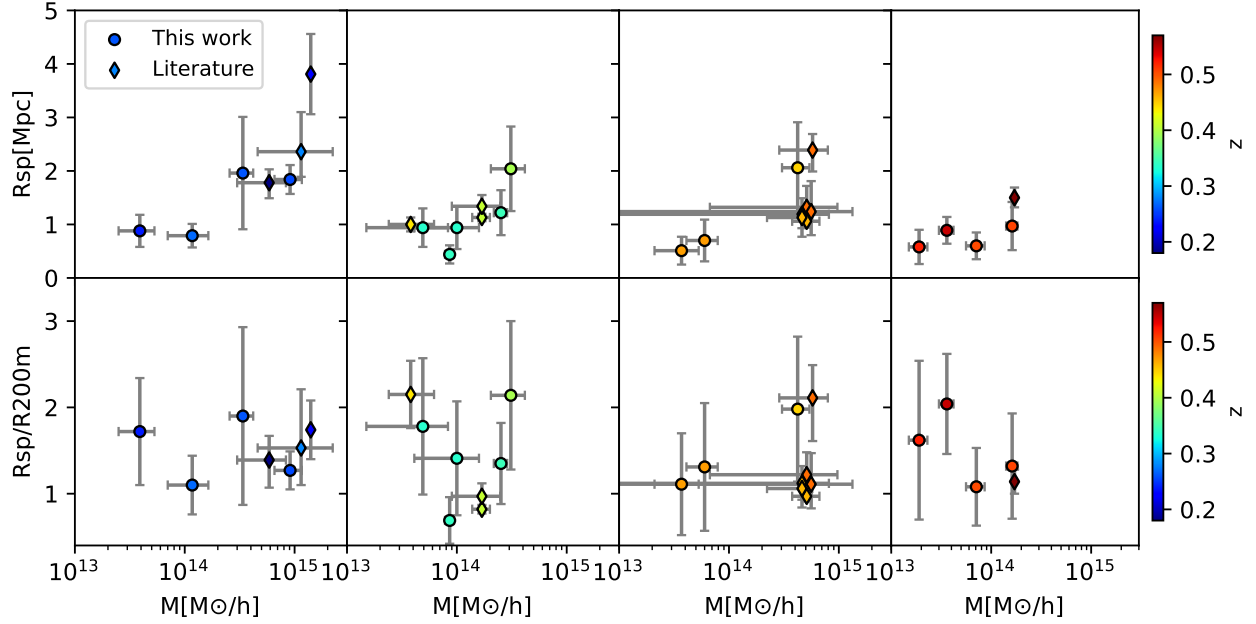


Figure 5. The relation between halo mass and the splashback radius (panels in the first row) or the normalized splashback radius (panels in the second row) in 4 redshift bins. In each row, from left to right, panels show halos from the low redshift to the high redshift. Measurements from this work and literature are shown with dots and diamonds, respectively. The color of the data point represents the redshift.

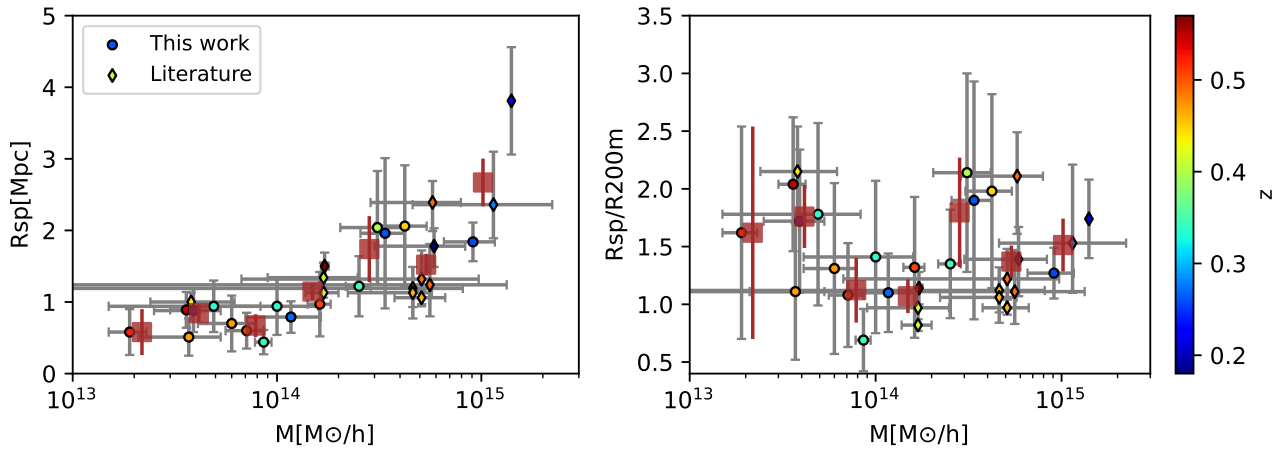


Figure 6. The relation between halo mass and the splashback radius (left panel) or the normalized splashback radius (right panel). Measurements from this work and literature are shown with dots and diamonds, respectively. The color of the data point represents the redshift. The whole sample is rebinned and shown in brown squares with errorbars.

1 We would like to thank the anonymous referee for
 2 detailed comments and suggestions, resulting in an
 3 improved version of the manuscript. This work
 4 is supported by National Key R&D Program of
 5 China No. 2022YFF0503403 and the Ministry
 6 of Science and Technology of China (grant Nos.
 7 2020SKA0110100). We acknowledge the support
 8 of National Nature Science Foundation of China
 9 (Nos 11988101,11773032,12022306,12203063), the sup-
 10 port from the Ministry of Science and Technology
 11 of China (grant Nos. 2020SKA0110100), the sci-
 12 ence research grants from the China Manned Space
 13 Project (Nos CMS-CSST-2021-B01,CMS-CSST-2021-

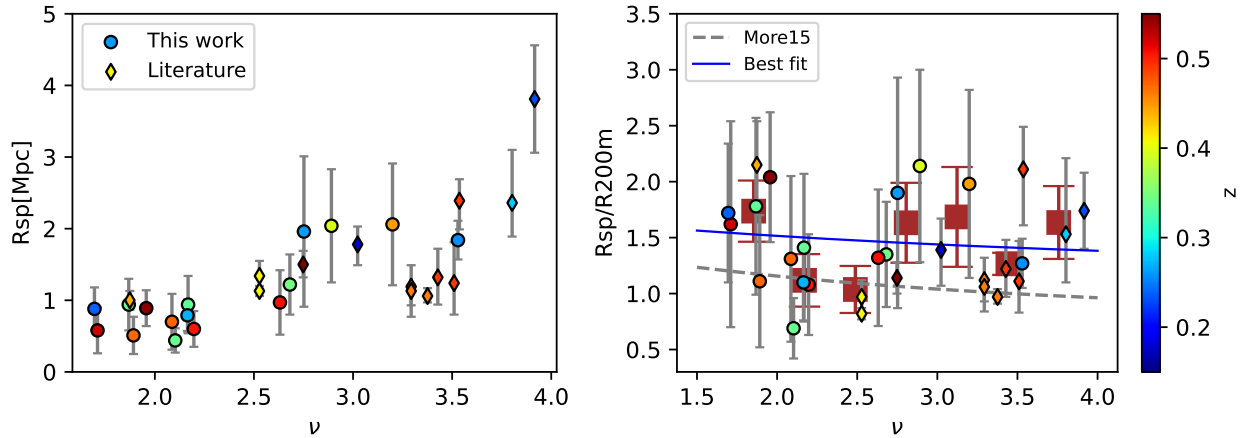


Figure 7. The relation between the peak height and splashback radius (left panel) and the normalized splashback radius (right panel). The symbols are the same with Fig. 6. The rebinned result of the whole sample is shown with the brown squares with corresponding errorbars. The model from More et al. (2015) is overlaid as the grey dashed curve, while the best-fit model is shown in the blue solid curve.

REFERENCES

- Adhikari, S., Dalal, N., & Chamberlain, R. T. 2014, JCAP, 2014, 019, doi: [10.1088/1475-7516/2014/11/019](https://doi.org/10.1088/1475-7516/2014/11/019)
- Adhikari, S., Dalal, N., & Clampitt, J. 2016, JCAP, 2016, 022, doi: [10.1088/1475-7516/2016/07/022](https://doi.org/10.1088/1475-7516/2016/07/022)
- Adhikari, S., Sakstein, J., Jain, B., Dalal, N., & Li, B. 2018, JCAP, 2018, 033, doi: [10.1088/1475-7516/2018/11/033](https://doi.org/10.1088/1475-7516/2018/11/033)
- Adhikari, S., Shin, T.-h., Jain, B., et al. 2021, ApJ, 923, 37, doi: [10.3847/1538-4357/ac0bbc10.48550/arXiv.2008.11663](https://doi.org/10.3847/1538-4357/ac0bbc10.48550/arXiv.2008.11663)
- Ahn, C. P., Alexandroff, R., Allende Prieto, C., et al. 2014, ApJS, 211, 17, doi: [10.1088/0067-0049/211/2/17](https://doi.org/10.1088/0067-0049/211/2/17)
- Aung, H., Nagai, D., & Lau, E. T. 2021, MNRAS, 508, 2071, doi: [10.1093/mnras/stab2598](https://doi.org/10.1093/mnras/stab2598)
- Banerjee, A., Adhikari, S., Dalal, N., More, S., & Kravtsov, A. 2020, JCAP, 2020, 024, doi: [10.1088/1475-7516/2020/02/024](https://doi.org/10.1088/1475-7516/2020/02/024)
- Baxter, E., Chang, C., Jain, B., et al. 2017, ApJ, 841, 18, doi: [10.3847/1538-4357/aa6ff010.48550/arXiv.1702.01722](https://doi.org/10.3847/1538-4357/aa6ff010.48550/arXiv.1702.01722)
- Bertschinger, E. 1985, ApJS, 58, 39, doi: [10.1086/191028](https://doi.org/10.1086/191028)
- Bianconi, M., Buscicchio, R., Smith, G. P., et al. 2021, ApJ, 911, 136, doi: [10.3847/1538-4357/abebd710.48550/arXiv.2010.05920](https://doi.org/10.3847/1538-4357/abebd710.48550/arXiv.2010.05920)
- Blum, R. D., Burleigh, K., Dey, A., et al. 2016, in American Astronomical Society Meeting Abstracts, Vol. 228, American Astronomical Society Meeting Abstracts #228, 317.01
- Challinor, A., & Lewis, A. 2011, PhRvD, 84, 043516, doi: [10.1103/PhysRevD.84.043516](https://doi.org/10.1103/PhysRevD.84.043516)
- Chang, C., Baxter, E., Jain, B., et al. 2018, ApJ, 864, 83, doi: [10.3847/1538-4357/aad5e7](https://doi.org/10.3847/1538-4357/aad5e7)
- Chue, C. Y. R., Dalal, N., & White, M. 2018, JCAP, 2018, 012, doi: [10.1088/1475-7516/2018/10/012](https://doi.org/10.1088/1475-7516/2018/10/012)
- Contigiani, O., Hoekstra, H., & Bahé, Y. M. 2019, MNRAS, 485, 408, doi: [10.1093/mnras/stz40410.48550/arXiv.1809.10045](https://doi.org/10.1093/mnras/stz40410.48550/arXiv.1809.10045)
- Contigiani, O., Hoekstra, H., Brouwer, M. M., et al. 2023, MNRAS, 518, 2640, doi: [10.1093/mnras/stac302710.48550/arXiv.2208.09369](https://doi.org/10.1093/mnras/stac302710.48550/arXiv.2208.09369)
- Coupon, J., Kilalinger, M., McCracken, H. J., et al. 2012, A&A, 542, A5, doi: [10.1051/0004-6361/201117625](https://doi.org/10.1051/0004-6361/201117625)
- Cuesta, A. J., Prada, F., Klypin, A., & Moles, M. 2008, MNRAS, 389, 385, doi: [10.1111/j.1365-2966.2008.13590.x](https://doi.org/10.1111/j.1365-2966.2008.13590.x)
- Dacunha, T., Belyakov, M., Adhikari, S., et al. 2022, MNRAS, 512, 4378, doi: [10.1093/mnras/stac392](https://doi.org/10.1093/mnras/stac392)
- Dark Energy Survey Collaboration, Abbott, T., Abdalla, F. B., et al. 2016, MNRAS, 460, 1270, doi: [10.1093/mnras/stw641](https://doi.org/10.1093/mnras/stw641)
- Deason, A. J., Oman, K. A., Fattahi, A., et al. 2021, MNRAS, 500, 4181, doi: [10.1093/mnras/staa3590](https://doi.org/10.1093/mnras/staa3590)
- Dey, A., Schlegel, D. J., Lang, D., et al. 2019, AJ, 157, 168, doi: [10.3847/1538-3881/ab089d](https://doi.org/10.3847/1538-3881/ab089d)
- Diemand, J., & Kuhlen, M. 2008, ApJL, 680, L25, doi: [10.1086/589688](https://doi.org/10.1086/589688)
- Diemer, B. 2018, ApJS, 239, 35, doi: [10.3847/1538-4365/aaee8c](https://doi.org/10.3847/1538-4365/aaee8c)
- . 2020, ApJS, 251, 17, doi: [10.3847/1538-4365/abfb51](https://doi.org/10.3847/1538-4365/abfb51)
- . 2022, MNRAS, 513, 573, doi: [10.1093/mnras/stac878](https://doi.org/10.1093/mnras/stac878)
- Diemer, B., & Kravtsov, A. V. 2014, ApJ, 789, 1, doi: [10.1088/0004-637X/789/1/1](https://doi.org/10.1088/0004-637X/789/1/1)

- Diemer, B., Mansfield, P., Kravtsov, A. V., & More, S. 2017, *ApJ*, 843, 140, doi: [10.3847/1538-4357/aa79ab](https://doi.org/10.3847/1538-4357/aa79ab)
- Diemer, B., More, S., & Kravtsov, A. V. 2013, *ApJ*, 766, 25, doi: [10.1088/0004-637X/766/1/25](https://doi.org/10.1088/0004-637X/766/1/25)
- Einasto, J. 1965, *Trudy Astrofizicheskogo Instituta Alma-Ata*, 5, 87
- Eisenstein, D. J., & Hu, W. 1998, *ApJ*, 496, 605, doi: [10.1086/305424](https://doi.org/10.1086/305424)
- Fillmore, J. A., & Goldreich, P. 1984, *ApJ*, 281, 1, doi: [10.1086/162070](https://doi.org/10.1086/162070)
- Fong, M., & Han, J. 2021, *MNRAS*, 503, 4250, doi: [10.1093/mnras/stab259](https://doi.org/10.1093/mnras/stab259)
- Fong, M., Han, J., Zhang, J., et al. 2022, *MNRAS*, 513, 4754, doi: [10.1093/mnras/stac1263](https://doi.org/10.1093/mnras/stac1263)
- Foreman-Mackey, D., Hogg, D. W., Lang, D., & Goodman, J. 2013a, *PASP*, 125, 306, doi: [10.1086/670067](https://doi.org/10.1086/670067)
- . 2013b, *PASP*, 125, 306, doi: [10.1086/670067](https://doi.org/10.1086/670067)
- Gao, L., Navarro, J. F., Cole, S., et al. 2008, *MNRAS*, 387, 536, doi: [10.1111/j.1365-2966.2008.13277.x](https://doi.org/10.1111/j.1365-2966.2008.13277.x)
- García, R., Salazar, E., Rozo, E., et al. 2023, *MNRAS*, 521, 2464, doi: [10.1093/mnras/stad660](https://doi.org/10.1093/mnras/stad660)
- Giblin, B., Heymans, C., Asgari, M., et al. 2021, *Astronomy & Astrophysics*, 645, A105, doi: [10.1051/0004-6361/202038850](https://doi.org/10.1051/0004-6361/202038850)
- Gunn, J. E., & Gott, J. Richard, I. 1972, *ApJ*, 176, 1, doi: [10.1086/151605](https://doi.org/10.1086/151605)
- Hildebrandt, H., Viola, M., Heymans, C., et al. 2017, *MNRAS*, 465, 1454, doi: [10.1093/mnras/stw2805](https://doi.org/10.1093/mnras/stw2805)
- Hoekstra, H., Franx, M., Kuijken, K., & van Dokkum, P. G. 2002, *MNRAS*, 333, 911, doi: [10.1046/j.1365-8711.2002.05479.x](https://doi.org/10.1046/j.1365-8711.2002.05479.x)
- Howlett, C., Lewis, A., Hall, A., & Challinor, A. 2012, *JCAP*, 1204, 027, doi: [10.1088/1475-7516/2012/04/027](https://doi.org/10.1088/1475-7516/2012/04/027)
- Jarvis, M., Sheldon, E., Zuntz, J., et al. 2016, *MNRAS*, 460, 2245, doi: [10.1093/mnras/stw990](https://doi.org/10.1093/mnras/stw990)
- Johnston, D. E., Sheldon, E. S., Wechsler, R. H., et al. 2007, *arXiv e-prints*, arXiv:0709.1159. <https://arxiv.org/abs/0709.1159>
- Klypin, A., Yepes, G., Gottlöber, S., Prada, F., & Heß, S. 2016, *MNRAS*, 457, 4340, doi: [10.1093/mnras/stw248](https://doi.org/10.1093/mnras/stw248)
- Lang, D., Hogg, D. W., & Schlegel, D. J. 2016, *AJ*, 151, 36, doi: [10.3847/0004-6256/151/2/36](https://doi.org/10.3847/0004-6256/151/2/36)
- Lange, J. U., Leauthaud, A., Singh, S., et al. 2021, *MNRAS*, 502, 2074, doi: [10.1093/mnras/stab189](https://doi.org/10.1093/mnras/stab189)
- Lewis, A., & Bridle, S. 2002, *PhRvD*, 66, 103511, doi: [10.1103/PhysRevD.66.103511](https://doi.org/10.1103/PhysRevD.66.103511)
- Lewis, A., Challinor, A., & Lasenby, A. 2000, *ApJ*, 538, 473, doi: [10.1086/309179](https://doi.org/10.1086/309179)
- Li, H., Zhang, J., Liu, D., et al. 2021, *ApJ*, 908, 93, doi: [10.3847/1538-4357/abcda3](https://doi.org/10.3847/1538-4357/abcda3)
- Ludlow, A. D., Navarro, J. F., White, S. D. M., et al. 2011, *MNRAS*, 415, 3895, doi: [10.1111/j.1365-2966.2011.19008.x](https://doi.org/10.1111/j.1365-2966.2011.19008.x)
- Mansfield, P., & Kravtsov, A. V. 2020, *MNRAS*, 493, 4763, doi: [10.1093/mnras/staa430](https://doi.org/10.1093/mnras/staa430)
- Mansfield, P., Kravtsov, A. V., & Diemer, B. 2017, *ApJ*, 841, 34, doi: [10.3847/1538-4357/aa7047](https://doi.org/10.3847/1538-4357/aa7047)
- McClintock, T., Varga, T. N., Gruen, D., et al. 2019, *MNRAS*, 482, 1352, doi: [10.1093/mnras/sty2711](https://doi.org/10.1093/mnras/sty2711)
- Melchior, P., Gruen, D., McClintock, T., et al. 2017, *MNRAS*, 469, 4899, doi: [10.1093/mnras/stx1053](https://doi.org/10.1093/mnras/stx1053)
- Miller, L., Kitching, T. D., Heymans, C., Heavens, A. F., & van Waerbeke, L. 2007, *MNRAS*, 382, 315, doi: [10.1111/j.1365-2966.2007.12363.x](https://doi.org/10.1111/j.1365-2966.2007.12363.x)
- Miller, L., Heymans, C., Kitching, T. D., et al. 2013, *MNRAS*, 429, 2858, doi: [10.1093/mnras/sts454](https://doi.org/10.1093/mnras/sts454)
- Moraes, B., Kneib, J. P., Leauthaud, A., et al. 2014, in *Revista Mexicana de Astronomia y Astrofisica Conference Series*, Vol. 44, *Revista Mexicana de Astronomia y Astrofisica Conference Series*, 202–203
- More, S., Diemer, B., & Kravtsov, A. V. 2015, *ApJ*, 810, 36, doi: [10.1088/0004-637X/810/1/36](https://doi.org/10.1088/0004-637X/810/1/36)
- More, S., Miyatake, H., Takada, M., et al. 2016, *ApJ*, 825, 39, doi: [10.3847/0004-637X/825/1/39](https://doi.org/10.3847/0004-637X/825/1/39)
- Murata, R., Sunayama, T., Oguri, M., et al. 2020, *PASJ*, 72, 64, doi: [10.1093/pasj/psaa04110.48550/arXiv.2001.01160](https://doi.org/10.1093/pasj/psaa04110.48550/arXiv.2001.01160)
- Navarro, J. F., Frenk, C. S., & White, S. D. M. 1996, *ApJ*, 462, 563, doi: [10.1086/177173](https://doi.org/10.1086/177173)
- Navarro, J. F., Hayashi, E., Power, C., et al. 2004, *MNRAS*, 349, 1039, doi: [10.1111/j.1365-2966.2004.07586.x](https://doi.org/10.1111/j.1365-2966.2004.07586.x)
- Navarro, J. F., Ludlow, A., Springel, V., et al. 2010, *MNRAS*, 402, 21, doi: [10.1111/j.1365-2966.2009.15878.x](https://doi.org/10.1111/j.1365-2966.2009.15878.x)
- O’Neil, S., Barnes, D. J., Vogelsberger, M., & Diemer, B. 2021, *MNRAS*, 504, 4649, doi: [10.1093/mnras/stab1221](https://doi.org/10.1093/mnras/stab1221)
- Phriksee, A., Jullo, E., Limousin, M., et al. 2020, *MNRAS*, 491, 1643, doi: [10.1093/mnras/stz3049](https://doi.org/10.1093/mnras/stz3049)
- Pizzardo, M., Geller, M. J., Kenyon, S. J., & Damjanov, I. 2023, *The Splashback Radius and the Radial Velocity Profile of Galaxy Clusters in IllustrisTNG*. <https://arxiv.org/abs/2311.10854>
- Planck Collaboration, Aghanim, N., Akrami, Y., et al. 2020, *A&A*, 641, A6, doi: [10.1051/0004-6361/201833910](https://doi.org/10.1051/0004-6361/201833910)
- Rohatgi, A. 2020, *Webplotdigitizer: Version 4.4*. <https://automeris.io/WebPlotDigitizer>
- Rykoff, E. S., Rozo, E., Busha, M. T., et al. 2014, *ApJ*, 785, 104, doi: [10.1088/0004-637X/785/2/104](https://doi.org/10.1088/0004-637X/785/2/104)
- Shi, X. 2016, *MNRAS*, 459, 3711, doi: [10.1093/mnras/stw925](https://doi.org/10.1093/mnras/stw925)

- Shin, T., Adhikari, S., Baxter, E. J., et al. 2019, MNRAS, 487, 2900, doi: [10.1093/mnras/stz143410.48550/arXiv.1811.06081](https://doi.org/10.1093/mnras/stz143410.48550/arXiv.1811.06081)
- Shin, T., Jain, B., Adhikari, S., et al. 2021, MNRAS, 507, 5758, doi: [10.1093/mnras/stab250510.48550/arXiv.2105.05914](https://doi.org/10.1093/mnras/stab250510.48550/arXiv.2105.05914)
- Smith, R. E., Peacock, J. A., Jenkins, A., et al. 2003, MNRAS, 341, 1311, doi: [10.1046/j.1365-8711.2003.06503.x](https://doi.org/10.1046/j.1365-8711.2003.06503.x)
- Takahashi, R., Sato, M., Nishimichi, T., Taruya, A., & Oguri, M. 2012, ApJ, 761, 152, doi: [10.1088/0004-637X/761/2/152](https://doi.org/10.1088/0004-637X/761/2/152)
- Villarreal, A. S., Zentner, A. R., Mao, Y.-Y., et al. 2017, MNRAS, 472, 1088, doi: [10.1093/mnras/stx2045](https://doi.org/10.1093/mnras/stx2045)
- Khakaj, E., Diemer, B., Leauthaud, A., et al. 2020, MNRAS, 499, 3534, doi: [10.1093/mnras/staa3046](https://doi.org/10.1093/mnras/staa3046)
- Yang, X., Xu, H., He, M., et al. 2021, ApJ, 909, 143, doi: [10.3847/1538-4357/abddb2](https://doi.org/10.3847/1538-4357/abddb2)
- Yao, J., Shan, H., Zhang, P., Kneib, J.-P., & Jullo, E. 2020, ApJ, 904, 135, doi: [10.3847/1538-4357/abc175](https://doi.org/10.3847/1538-4357/abc175)
- Yao, J., Shan, H., Zhang, P., et al. 2023a, arXiv e-prints, arXiv:2301.13437, doi: [10.48550/arXiv.2301.13437](https://doi.org/10.48550/arXiv.2301.13437)
- . 2023b, arXiv e-prints, arXiv:2301.13434, doi: [10.48550/arXiv.2301.13434](https://doi.org/10.48550/arXiv.2301.13434)
- Zou, H., Gao, J., Zhou, X., & Kong, X. 2019, ApJS, 242, 8, doi: [10.3847/1538-4365/ab1847](https://doi.org/10.3847/1538-4365/ab1847)
- Zou, H., Gao, J., Xu, X., et al. 2021, ApJS, 253, 56, doi: [10.3847/1538-4365/abe5b0](https://doi.org/10.3847/1538-4365/abe5b0)
- Zu, Y., Shan, H., Zhang, J., et al. 2021, MNRAS, 505, 5117, doi: [10.1093/mnras/stab1712](https://doi.org/10.1093/mnras/stab1712)
- Zuntz, J., Sheldon, E., Samuroff, S., et al. 2018, MNRAS, 481, 1149, doi: [10.1093/mnras/sty2219](https://doi.org/10.1093/mnras/sty2219)
- Zürcher, D., & More, S. 2019, ApJ, 874, 184, doi: [10.3847/1538-4357/ab08e810.48550/arXiv.1811.06511](https://doi.org/10.3847/1538-4357/ab08e810.48550/arXiv.1811.06511)